日本磁気学会
ISSN 2432-0250
Journal of the Magnetics Society of Japan
Electronic Journal URL: https://www.jstage.jst.go.jp/browse/msjmag

Vol.44 No.6　2020

Journal

JOURNAL OF THE MAGNETICS SOCIETY OF JAPAN

Vol.44 No.6 2020

日本磁気学会

ISSN 2432-0250

HP: http://www.magnetics.jp/ e-mail: msj@bj.wakwak.com

Electronic Journal: http://www.jstage.jst.go.jp/browse/msjmag

世界初！
高温超電導型VSM

新製品

世界初*、高温超電導マグネットをVSMに採用することで
測定速度 当社従来機1/20を実現。
0.5mm cube磁石のBr, HcJ高精度測定が可能と
なりました。
*2014年7月 東英工業調べ

測定結果例

高温超電導VSMによるNdFeB(sint.) 0.5mm cube BHカーブ

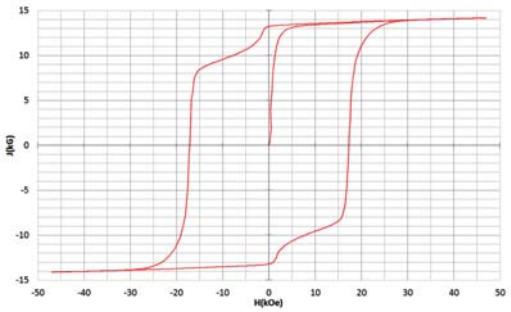

磁化測定レンジ：0.2emu
Br = 13.2kG　　HcJ = 17.2kOe

高温超電導VSMによるNdFeB(sint.) 1mm cube BHカーブ

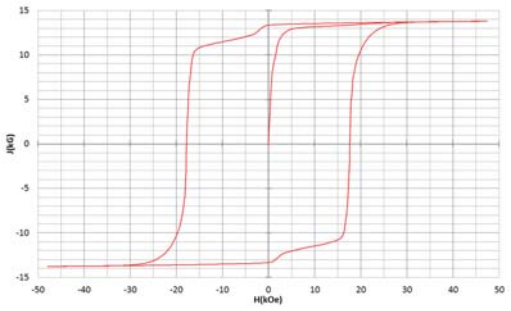

磁化測定レンジ：2emu
Br = 13.3kG　　HcJ = 17.7kOe

高温超電導VSMによるNdFeB(sint.) 4mm cube BHカーブ

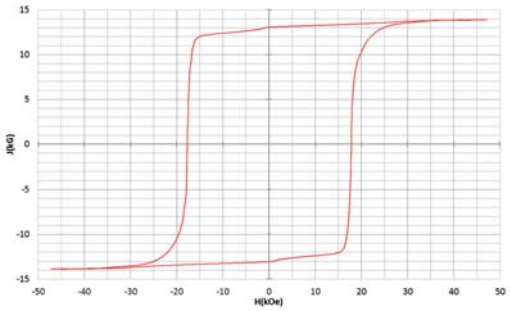

磁化測定レンジ：100emu
Br = 13.1kG　　HcJ = 17.8kOe

高速測定を実現

高温超電導マグネット採用により、高速測定を実現しました。Hmax= 5Tesla, Full Loop 測定が2分で可能です。
（当社従来機：Full Loop測定　40分）

小試料のBr,HcJ高精度測定

0.5mm cube 磁石のBr,HcJ高精度測定ができ、表面改質領域を切り出しBr,HcJの強度分布等、微小変化量の比較測定が可能です。
また、試料の加工劣化の比較測定が可能です。

試料温度可変測定

−50℃～+200℃温度可変UNIT（オプション）

磁界発生部の小型化

マグネットシステム部寸法：0.8m×0.3m×0.3m

TOEI 東英工業株式会社
http://www.toeikogyo.co.jp
〒194-0035 東京都町田市忠生1-8-13
TEL：042-791-1211 FAX：042-792-0490
E-mail : sales@toeikogyo.co.jp

Journal of the Magnetics Society of Japan
Vol. 44, No. 6

Electronic Journal URL: https://www.jstage.jst.go.jp/browse/msjmag

CONTENTS

J. Magn. Soc. Jpn., **44**, 129-132 (2020)

Letter

Iron loss and hysteresis properties of nanocrystalline magnetic materials under high frequency inverter excitation

A. Yao, F. Kato, and H. Sato
National Institute of Advanced Industrial Science and Technology (AIST), *16-1, Tsukuba 305-8569, Japan, a.yao@aist.go.jp*

Recently, wide-bandgap (WBG) power semiconductors made of silicon carbide (SiC) and gallium nitride (GaN) have been widely developed as high-speed switching devises. Many researchers have studied novel magnetic materials, such as nanocrystalline magnetic materials (NMMs), for low-loss electric motors and transformers. This study experimentally examines the hysteresis (*B*–*H*) curve and iron loss properties of the NMM core excited using a pulse width modulation (PWM) inverter at high carrier frequencies on the order of MHz with and without the dead time. For comparison, the magnetic properties of amorphous magnetic materials (AMMs) core are also evaluated. Particularly at high carrier frequencies (approximately 1 MHz), the iron loss of NMM and AMM cores significantly depends on the dead time. Compared with the case of the AMM core, the NMM core suppresses the increasing rate of iron losses caused by the dead time because the area of minor loops in NMM becomes small, particularly in high-frequency regions.

Key words: Nanocrystalline magnetic materials, iron loss, *B*–*H* curve, inverter, high frequency, wide-bandgap semiconductor

1 Introduction

Transformer and motor systems often comprise inverters and cores composed of soft magnetic materials. In motor systems, pulse width modulation (PWM) inverters are commonly used to perform speed and torque control. Thus, magnetic material cores are excited using a PWM inverter. The waveform generated using the PWM inverter exhibits high-order harmonic components and induces complex hysteresis (*B*–*H*) curves in soft magnetic material (motor) cores[1–17]. Owing to these complex hysteresis (*B*–*H*) curves of the cores, the iron loss under PWM inverter excitation increases by approximately 10%–50% compared with that under sinusoidal excitation[2]. The objective of this study is to clarify the complex hysteresis (*B*–*H*) curve and iron loss properties of nanocrystalline magnetic materials (NMMs)[18,19] core fed using the PWM inverter at the MHz high carrier frequency.

Recently, several researchers have focused on motor cores composed of NMM and amorphous magnetic materials (AMMs) to perform iron loss reduction[9,12,20,21]. NMM and AMM have lower iron loss density than conventional nonoriented (NO) silicon steel[11,12,21]. Moreover, a previous study has shown that the iron loss of the NMM motor is smaller than that of the AMM motor, and the NMM motor core is expected to be suitable for use in high-speed and high-frequency regions[12]. The iron loss characterization of NMM cores under high carrier frequency excitation using the inverter is useful for core design in high-speed and high-frequency regions. Therefore, examining the fundamental magnetic properties in the NMM core under high carrier frequency inverter excitation is necessary.

Wide-bandgap (WBG) power semiconductors made of silicon carbide (SiC) and gallium nitride (GaN) have been widely developed and studied as high-voltage, low loss, and particularly high speed switching devises[10,11]. Recently, using these WBG devices, magnetic properties of conventional NO silicon steel cores have been shown under PWM inverter excitation at high carrier frequencies on the order of MHz and without the dead time[17]. To use inverters that employ WBG devices, the next step is to understand the hysteresis (*B*–*H*) curve and iron loss properties of the NMM core under MHz high carrier frequency inverter excitation with and without the dead time. In the PWM inverter, the dead time is necessary for practical use to prevent a short circuit between the upper and lower arms.

This study experimentally examines the hysteresis (*B*–*H*) curve and iron loss properties of the NMM core excited using a GaN inverter at the MHz high carrier frequency. For comparison, the magnetic properties of the AMM core are also evaluated. Moreover, the impact of dead time on the magnetic properties of NMM and AMM cores excited using the high carrier frequency inverter with and without the dead time is discussed. When the ratio of the iron loss caused by the dead time to the total iron loss becomes small, the magnetic material is suitable for high-speed and high-frequency applications.

2 Experimental Method

Figure 1 illustrates a schematic of the ring core, single-phase GaN inverter, and measurement system to obtain the hysteresis (*B*–*H*) curve and iron loss properties. The ring core with a thickness of 7 mm, inner diameter of 102 mm, and outer diameter of 127 mm is composed of NMM (FT-3M) laminations[11]. For comparison, the ring core with identical geometries of AMM (SA-1) laminations is also used. Both ring laminations (NMM and AMM) are impregnated with acrylic resin and cut using the same wire-cutting technique. The stacking factor S_f of NMM and AMM ring cores is 0.873 and 0.935, respectively. These two ring cores have two (primary and secondary) coils that are wound using a wire. Here, the primary (secondary) coil is used as the exciting coil (*B*-coil to measure the magnetic flux density *B*). See Refs.[10,11,15,16] for further explanation of the ring cores.

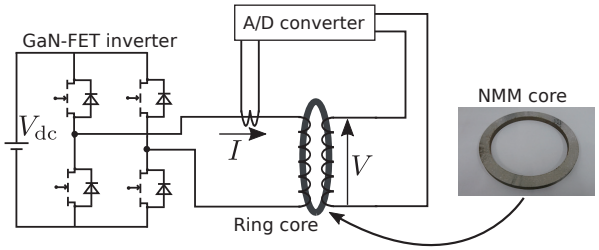

Fig. 1 Schematic of the NMM ring core, single-phase GaN inverter, and measurement system used to obtain the hysteresis (*B*–*H*) curve and iron loss characteristics.

The single-phase inverter with GaN field-effect transistors (GaN-FET)[10,17] is used to measure the hysteresis (*B*–*H*) curve and iron loss properties of two (NMM and AMM) ring cores. The frequency f_0 of the fundamental sinusoidal waveform is set to 50 Hz. The carrier frequency f_c of the triangular carrier waveform is varied from 400 kHz to 1.0 MHz in 200-kHz steps. The modulation index is defined as the ratio of the fundamental waveform to the carrier frequency waveform amplitude and is set at 0.7. The maximum magnetic flux density B_{max} of two ring cores is set at 0.5 T. The dead time D is set at 0, 10, and 20 ns.

To estimate the magnetic field intensity H (= $N_1 I/l$) and the magnetic flux density B (= $\int V\mathrm{d}t/(N_2 S_c S_f)$) in ring cores, the primary current I flowing through the primary winding and the B-coil voltage V induced in the secondary winding are measured. Here, N_1 (= 10) denotes the number of turns in the primary coil, l (= 0.36 m) is the magnetic path length of the ring cores, N_2 (= 10) is the number of turns in the secondary coil, and S_c (= 87.5 mm^2) is the cross-sectional area of the cores. To measure I and V, a current probe (HIOKI E.E. Corp., CT6711), a voltage probe (Iwatsu Electric Co., Ltd., SS-320), and a high-performance A/D converter (NI Corp., PXIe-5163, 14 bit, 1 GS/s) are used. Using H and B, the iron loss W of the ring cores can be calculated by[17]

$$W = \frac{f_0}{\rho}\int H\mathrm{d}B, \tag{1}$$

where ρ denotes the density of the cores. Here, ρ of NMM and AMM is 7300 and 7180 kg/m^3, respectively.

To clarify the impact of the increasing rate of iron loss caused by the dead time, the ratio η_n of the loss without the dead time to that with the dead time is discussed. Here, η_n is defined by the following equation:

$$\eta_n = \frac{W_n}{W_0}, \tag{2}$$

where W_0 denotes the iron loss without the dead time and W_n is that with the dead time. In this study, n (W_n) can be set to either 10 or 20 ns (W_{10} or W_{20}).

3 Results and Discussion

Figures 2 and 3 show the hysteresis (*B*–*H*) curves at f_c = 400 kHz and 1.0 MHz when the NMM and AMM ring cores are excited using the GaN inverter at D = 0, 10, and 20 ns. Owing to the high-harmonic components, the PWM carrier waveform is responsible for many minor loops in the hysteresis (*B*–*H*) curves (See Refs.[10,11] for the further explanation of the minor loops). In Ref.[17], the hysteresis (*B*–*H*) curve and its minor loop of the conventional NO silicon steel core fed using an inverter under carrier frequencies on the order of MHz without the dead time were observed. For the first time, this study shows that the NMM and AMM cores also have minor loops under inverter excitation at a relatively high carrier frequency of 1 MHz. As shown in Figs. 2 and 3, the width and area of the minor loops in both NMM and AMM cores increase with an increase in the dead time. It is assumed that owing to the dead time, the return current becomes large[4]; then, the change in the minor loop becomes large (See Refs.[4,14] for further explanation of the relationship between the dead time and the minor loop.). Under inverter excitation, the width and area of the minor loops of NMM become small compared with those of AMM. There are two possible reasons for these phenomena. First, H of the major loop in the NMM core is smaller than that in the AMM core; then, the variation in H of the minor loop of NMM condenses. Second, because the thickness of the NMM sheet (approximately 18 μm) is thinner than that of the AMM sheet (approximately 25 μm), the eddy current loss of NMM becomes small compared with that of AMM; then, the area of the minor loops of NMM becomes small.

Figure 4 shows the carrier frequency dependence of iron losses in the two ring cores under inverter excitation at D = 0, 10, and 20 ns. Each iron loss (W) is obtained from the average of five measurements. The error bars (standard deviation) of each measurement are shown. W at D = 0 ns in these two cores decreases with respect to f_c up to approximately 800 kHz and then increases. W at D = 10 and 20 ns in the NMM core monotonically increases with an increase in f_c. W at D = 10 and 20 ns in the AMM core almost reaches the minimum value when f_c is 600 kHz. These results indicate that when the dead time increases, the carrier frequency at which the iron loss reaches the minimum value shifts to the low-frequency side. A previous study has shown that owing to the skin effect and the distortion of the input voltage, W decreases and increases with an increase in f_c on the order of MHz[17]. This study shows that particularly at such high carrier frequencies (f_c = approximately 1 MHz), the iron loss of the NMM and AMM cores not only depends on the skin effect and the distortion of the input voltage but also significantly depends on the dead time.

Finally, the impact of increased iron loss owing to the dead time of the NMM and AMM cores excited using a PWM inverter under high carrier frequencies on the order of MHz is discussed. Figure 5 shows the ratio η_n with respect to f_c using Eq. (2). As shown in this figure, η_n monotonically increases with an increase in f_c. In the high carrier frequency region, the impact of the dead time on one pulse becomes large; then, the minor loop in the case with the dead time increases compared with the case without the dead time, as shown in Figs. 2 and 3. Here, η_{10} and η_{20} of the

NMM ring core are smaller than those of the AMM core. Thus, the increasing rate of loss owing to the dead time in the NMM ring core is smaller than that in the AMM core. It is assumed that this occurs because under inverter excitation, the area of the minor loops of NMM becomes small compared with that of AMM, as shown in Figs. 2 and 3. Therefore, for the first time, this study shows that the NMM core can have a low iron loss caused by the fundamental waveform and suppress the increasing rate of iron losses caused by the dead time compared with the case of the AMM core, particularly in the high carrier frequency region. The NMM core is expected to be suitable for use in motor and power converter systems using WBG devices, such as SiC and GaN, in high-speed and high-frequency regions, in which the influence of the dead time becomes large.

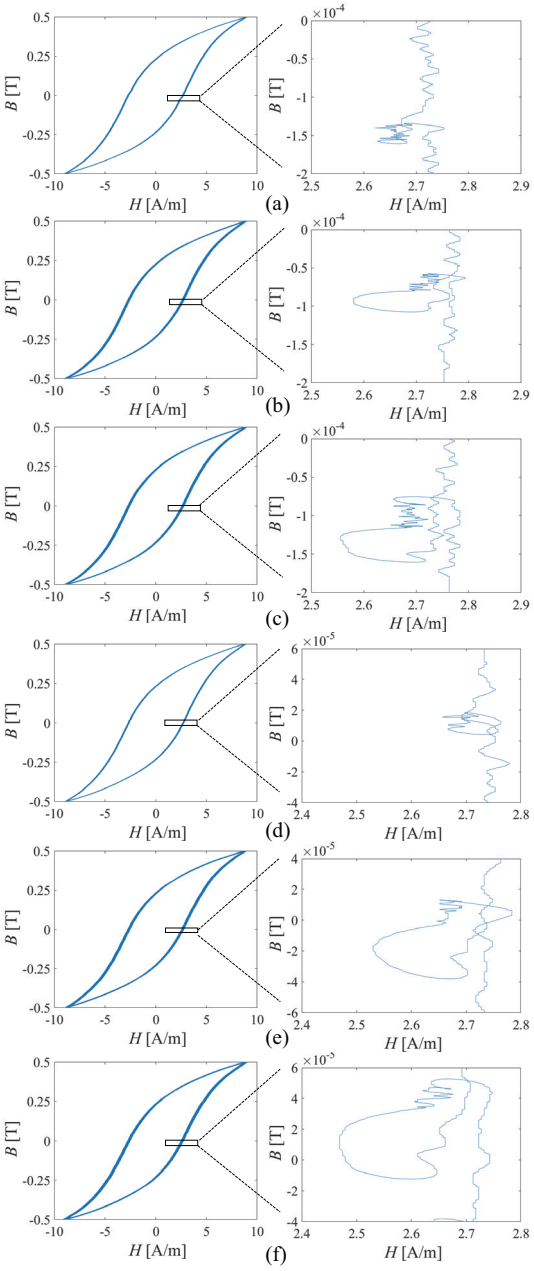

Fig. 2 Hysteresis (B–H) curves of the NMM ring core fed using a PWM inverter. The left panels show the major loops, and right panels show the minor loops, which correspond to the enlarged view of the part of the left panels. (a) f_c = 400 kHz and D = 0 ns, (b) f_c = 400 kHz and D = 10 ns, (c) f_c = 400 kHz and D = 20 ns, (d) f_c = 1 MHz and D = 0 ns, (e) f_c = 1 MHz and D = 10 ns, and (f) f_c = 1 MHz and D = 20 ns

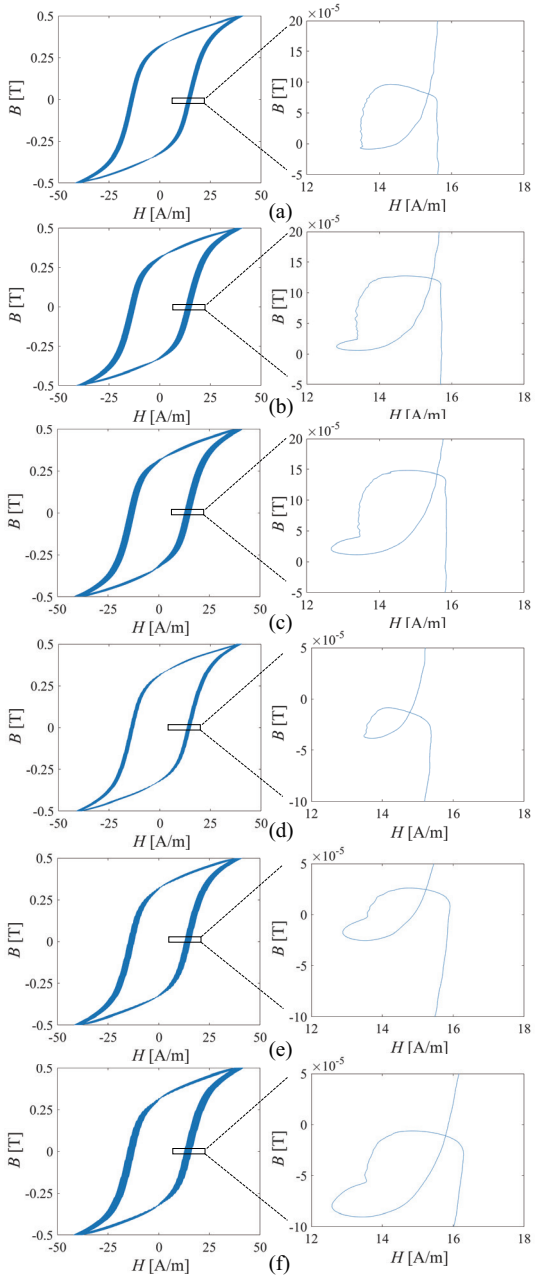

Fig. 3 Hysteresis (B–H) curves of the AMM ring core fed using a PWM inverter. The left panels show the major loops, and right panels show the minor loops, which correspond to the enlarged view of the part of the left panels. (a) f_c = 400 kHz and D = 0 ns, (b) f_c = 400 kHz and D = 10 ns, (c) f_c = 400 kHz and D = 20 ns, (d) f_c = 1 MHz and D = 0 ns, (e) f_c = 1 MHz and D = 10 ns, and (f) f_c = 1 MHz and D = 20 ns

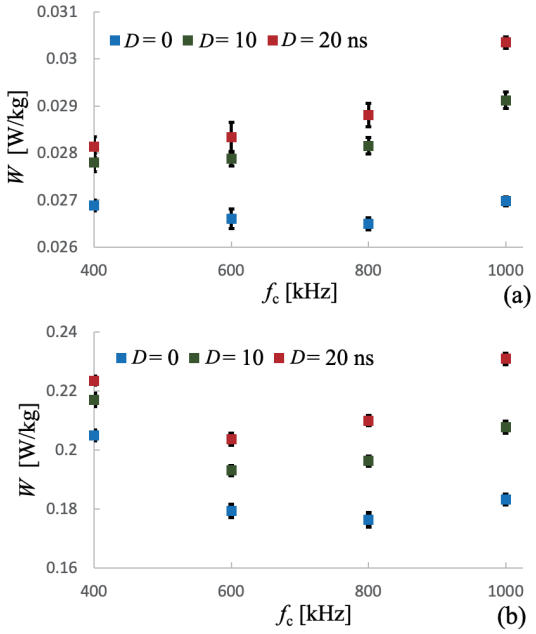

Fig. 4 Carrier frequency dependence of iron losses in the two ring cores under PWM inverter excitation at D = 0, 10, and 20 ns: (a) NMM and (b) AMM

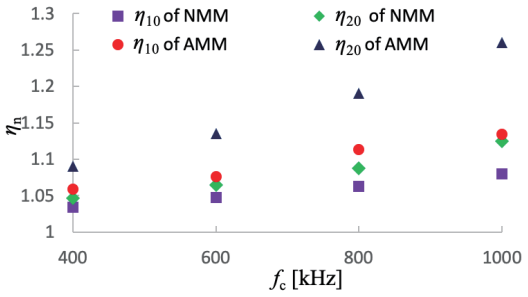

Fig. 5 Ratio η_n of loss without the dead time to that with the dead time as a function of f_c using Eq. (2).

4 Conclusions

This study experimentally examined the hysteresis (B–H) curve and iron loss properties of the NMM core excited using a PWM inverter at high carrier frequencies on the order of MHz with and without the dead time. Here, the AMM core was compared with the NMM core to discuss the magnetic properties of the NMM core. For the first time, this study showed that the NMM core suppressed an increasing rate of iron losses caused by the dead time compared with the case of the AMM core because the area of the minor loops of NMM became small, particularly in the high-frequency region. Thus, it is considered important to make the main loop small and the thickness of magnetic materials thin while developing magnetic materials. These results provide a path for further research on the iron loss reduction of magnetic materials under PWM inverter excitation at high carrier frequencies in motor and power converter systems using WBG devices, such as SiC and GaN. In the future, the loss repartition[9,16] at high carrier frequencies will be quantitatively evaluated by numerical simulations.

Acknowledgments This work was partly supported by the JSPS KAKENHI ♯20K14721, the JFE 21st Century Foundation, and the Nagamori Foundation Research Grant.

References

1) A. Boglietti, P. Ferraris, M. Lazzari, and F. Profumo: *IEEE Trans. Magn.*, **27**, 5334 (1991).
2) K. Fujisaki and S. Liu: *J. Appl. Phys.*, **115**, 17A321 (2014).
3) T. Taitoda, Y. Takahashi, and K. Fujiwara: *IEEE Trans. Magn.*, **51**, 1 (2015)
4) T. Tanaka, S. Koga, R. Kogi, S. Odawara, and K. Fujisaki: *IEEJ J. Ind. Appl.*, **136**, 110 (2016) (in Japanese).
5) W. Martinez, S. Odawara, and K. Fujisaki: *IEEE Trans. Magn.*, **53**, 1 (2017).
6) A. Yao, K. Tsukada, S. Odawara, K. Fujisaki, Y. Shindo, N. Yoshikawa, and T. Yoshitake: *AIP Adv.*, **7**, 056618 (2017).
7) A. Yao, T. Sugimoto, S. Odawara, and K. Fujisaki: *AIP Adv.*, **8**, 056804 (2018).
8) A. Yao, S. Odawara, and K. Fujisaki: *IEEJ J. Ind. Appl.*, **7**, 298 (2018).
9) A. Yao, T. Sugimoto, S. Odawara, and K. Fujisaki: *IEEE Trans. Magn.*, **54**, 1 (2018).
10) A. Yao, K. Tsukada, and K. Fujisaki: *IEEJ J. Ind. Appl.*, **7**, 321 (2018).
11) A. Yao, T. Sugimoto, and K. Fujisaki: *IEEJ J. Ind. Appl.*, **139**, 276 (2019) (in Japanese).
12) A. Yao, T. Sugimoto, and K. Fujisaki: *J. Magn. Soc. Jpn.*, **43**, 42 (2019).
13) A. Yao and T. Hatakeyama: *J. Magn. Soc. Jpn.*, **43**, 46 (2019).
14) A. Yao, T. Funaki, and T. Hatakeyama: *J. Magn. Soc. Jpn.*, **43**, 105 (2019).
15) A. Yao: *J. Magn. Soc. Jpn.*, **44**, 30 (2020).
16) A. Yao, R. Moriyama, and T. Hatakeyama: *J. Magn. Soc. Jpn.*, **44**, 52 (2020).
17) A. Yao, R. Moriyama, and T. Hatakeyama: *J. Magn. Soc. Jpn.*, **44**, 87 (2020).
18) Y. Yoshizawa and K. Yamauchi: *Mater. Trans., JIM*, **31**, 307 (1990).
19) A. Yao, M. Inoue, K. Tsukada, and K. Fujisaki: *AIP Adv.*, **8**, 056640 (2018).
20) N. Nishiyama, K. Tanimoto, and A. Makino: *AIP Adv.*, **6**, 055925 (2016).
21) N. Denis, M. Inoue, K. Fujisaki, H. Itabashi, and T. Yano: *IEEE Trans. Magn.*, **53**, 1 (2017).

Recieved Jul. 24, 2020; Accepted Sep. 4, 2020

J. Magn. Soc. Jpn., **44**, 133-136 (2020)

Letter

Chromatic aberration effect in refraction of spin waves

Tian Li*, Takuya Taniguchi**, Yoichi Shiota*, Takahiro Moriyama*, and Teruo Ono*, ***

*Institute for Chemical Research, Kyoto University, *Uji, Kyoto 611-0011, Japan*

**Fakultät für Physik, Technische Universität München, *Garching 85748, Germany*

***Center for Spintronics Research Network (CSRN), Graduate School of Engineering Science, Osaka University, *Osaka 560-8531, Japan*

We numerically investigated the refraction property of spin waves (SWs) at thickness step in films with out-of-plane magnetization, in which the SWs propagate isotropically in the film plane. It was confirmed the isotropic SWs were refracted at a thickness step by following the Snell's law. We also found that the refraction angle of SWs of the dipole-exchange mode depends on the resonant frequency, indicating that the chromatic aberration effect should be taken into account in designing magnonic devices.

Key words: magnonics, spin waves

Magnonics is a rapidly developing research field, in which spin waves (SWs) are utilized to transfer and process information[1-4]. In magnonics, controlling the propagation direction of SWs is one of the crucial issues[5-9]. It has been recently demonstrated that refraction is also useful for controlling the propagation direction of SWs[12,13,16-18]. In optics, the dispersion relation of light is isotropic, and thus, the relation between the incident and refraction angles is determined by the ratio of the refractive indices. On the other hand, for spin waves in thin films with in-plane magnetization the dispersion relation is anisotropic, and thus, deviations from Snell's law in optics has been reported[13, 16]. This deviation from Snell's law in optics results in the complicated design for magnonic devices[11]. Thus, isotropic SWs, rather than anisotropic SWs, are expected to be more suitable for application. Here, we numerically investigate the refraction property of SWs in thin films with perpendicular magnetization, in which the isotropic SW propagation in the film plane is expected from the symmetry. It is found that the refraction of SWs follows the Snell's law in optics with the chromatic aberration effect.

The micromagnetic simulation is performed utilizing mumax3[19]. In simulation, we use the following material parameters reported for yttrium iron garnet (YIG); the saturation magnetization $M_s = 139\,\mathrm{kA/m}$, the exchange stiffness $A_{ex} = 4.15\,\mathrm{pJ/m}$, and the Gilbert damping constant 1×10^{-4} [20,21]. In this study, two types of samples, labeled as sample A and B, are designed. Both samples are shaped as displayed in Fig. 1(a) and consist of thicker and thinner regions. The thicknesses of thicker and thinner areas are set to be 800 nm and 400 nm in sample A, and set to be 100 nm and 50 nm in sample B, respectively. The cell size for the calculation is $200 \times 200 \times 200\,\mathrm{nm^3}$ in sample A and $50 \times 50 \times 50\,\mathrm{nm^3}$ in sample B. Note that the cell size is set to be much smaller than the wavelength of excited SWs. To avoid the SW reflections at the edges of calculation area, the damping constants in the areas of 6 μm width from the left and right edges are set to increase gradually to 1. An external magnetic field $\mu_0 H_{ext} = 200\,\mathrm{mT}$ is applied to +z direction, which is enough to saturate the magnetization to z direction, and SWs are excited by locally applied rf field $\mu_0 H_{rf} \sin(2\pi f t)$ along x direction at an antenna in the thicker area. In this work, we use $\mu_0 H_{rf} = 1\,\mathrm{mT}$ and the frequency f of rf field is varied as f= 0.9, 1.0, and 1.1 GHz. We analyze the results recorded at 100 ns after the SW excitation.

Fig. 1(b) shows a typical result, which displays the phase of magnetization precession at each position in xy-plane. A SW with wavenumber k_1 propagates from the antenna to the thickness step with the incident angle θ_1 and it is refracted into the other SW with wavenumber k_2 at the thickness step with the refraction angle θ_2. The estimation of k_1, k_2, and θ_2 is accomplished as follows. Firstly, we define two areas (A1 and A2) and perform two-dimensional fast Fourier transform (2D-FFT) on the data in each area. Results of 2D-FFT are shown in Figs. 1(c) and 1(d). Secondly, we estimate k_1, which is the incident wavenumber in +x direction, from the data on $k_y = 0$ (Fig. 1(c)). k_1 is given as the second highest peak, as shown in Fig. 1(e). Thirdly, we linearly fit the 2D-FFT results of A2 and obtain θ_2 from the slope (Fig. 1(d)). Finally, k_2 is estimated from the second highest peak on the fitted line, as shown in Fig. 1(f).

To confirm that SWs propagate isotropically in both samples, we plot k_1 and k_2 as a function of θ_1, as shown in Fig. 2. Both k_1 and k_2 are almost constant with respect to θ_1 even if the resonant frequency is varied from 0.9 GHz to 1.1 GHz. If the SW dispersion relation is anistropic in the film plane, the wavenumber should depend on the SW propagating dicrections[13]. Therefore, the results shown in Fig. 2 indicates that the SWs propagate isotropically in both thicker and thinner regions, and Snell's law in optics, $\sin\theta_1 / \sin\theta_2 = k_2 / k_1$, can be applied in the present system.

It is known that the dispersion relation of SW

propagating in a film with perpendicular magnetization can be described as

$$\omega^2 = \left(\omega_H + \frac{2A_{\mathrm{ex}}\gamma}{M_s}k^2\right)\left[\omega_H + \frac{2A_{\mathrm{ex}}\gamma}{M_s}k^2 + \omega_M\left(1 - \frac{1-e^{-kd}}{kd}\right)\right] \quad (1)$$

where ω is the angular frequency of the excited SW, $\omega_H = \mu_0\gamma(H_{\mathrm{ext}} - M_{\mathrm{s}})$, $\omega_M = \mu_0\gamma M_{\mathrm{s}}$, μ_0 is the permeability of vacuum, γ is the gyromagnetic ratio, and d is the film thickness[10, 22]. Here, both dipole-dipole interaction and exchange interaction are taken into account. In the small-k limit (i.e. for magnetostatic SWs), where k^2 is comparatively smaller than kd, the influence of exchange interaction can be ignored. In that case, the SW dispersion relation for out-of-plane magnetized films, named as magnetostatic forward volume wave (MSFVW), is expressed as

$$\omega^2 = \omega_H\left[\omega_H + \omega_M\left(1 - \frac{1-e^{-kd}}{kd}\right)\right]. \quad (2)$$

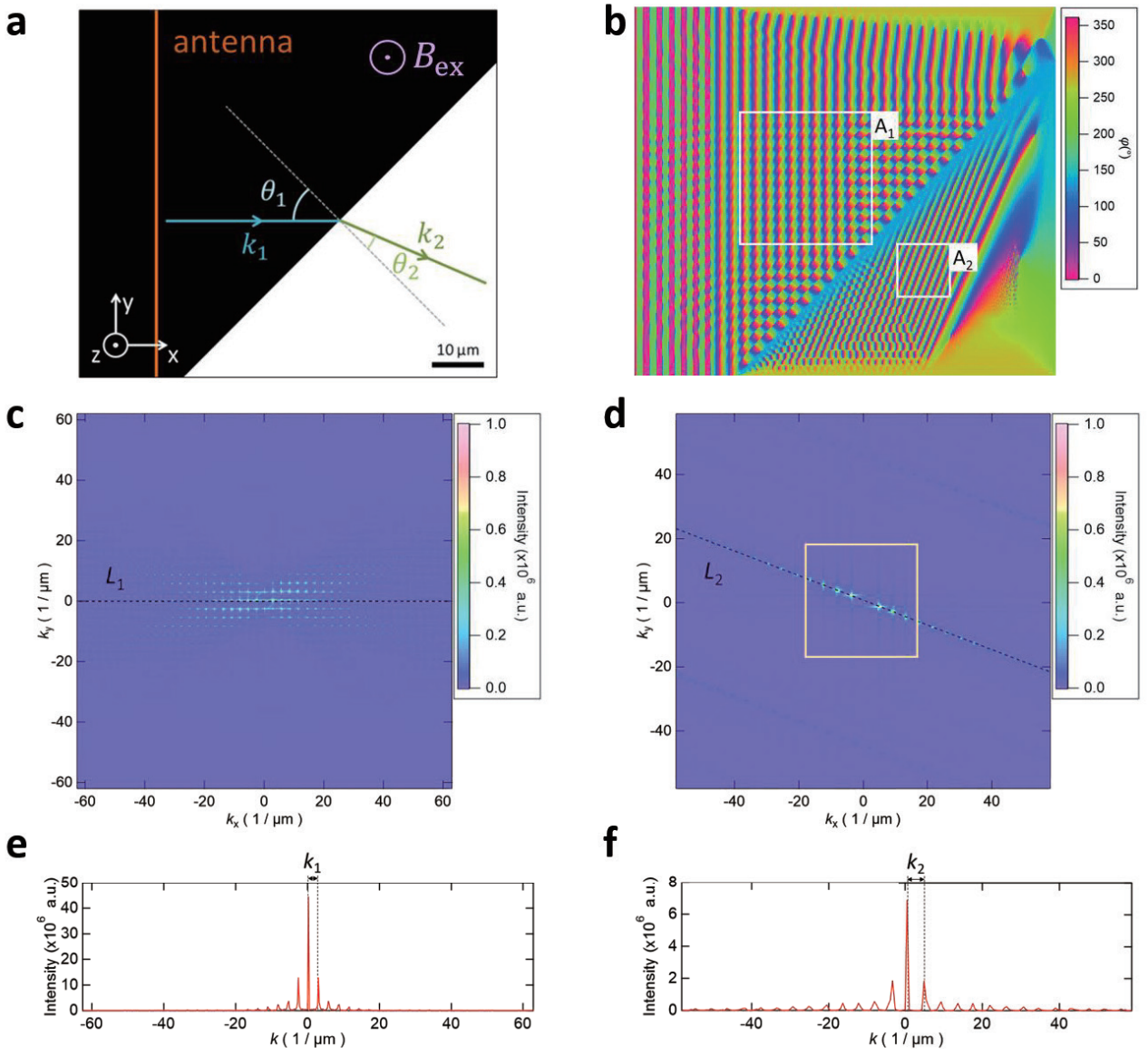

Fig.1 Example of process of simulation and analysis. The shown results are obtained from sample B when we set $f = 1$ GHz and $\theta_1 = 45°$. (a) Typical simulation setup. The black and white areas are respectively the thicker and thinner regions. The thickness step (boundary between two regions) is tilted with the angle θ_1. The rf magnetic field is applied at the antenna (orange line), which has one-cell width. k and θ of incident and refracted SWs are described by the blue and green arrows, respectively. (b) Simulation result of the SW propagation. The phase of magnetization precession, φ, is displayed. The areas A_1 and A_2 surrounded by white frames are utilized for analysis. (c,d) Results of 2D-FFT from (c) A_1 and (d) A_2. The black dashed line L_1 in (c) is $k_y = 0$ and L_2 in (d) is the result of linear fitting of intensity in the yellow frame. (e,f) Intensity on (e) L_1 and (f) L_2.

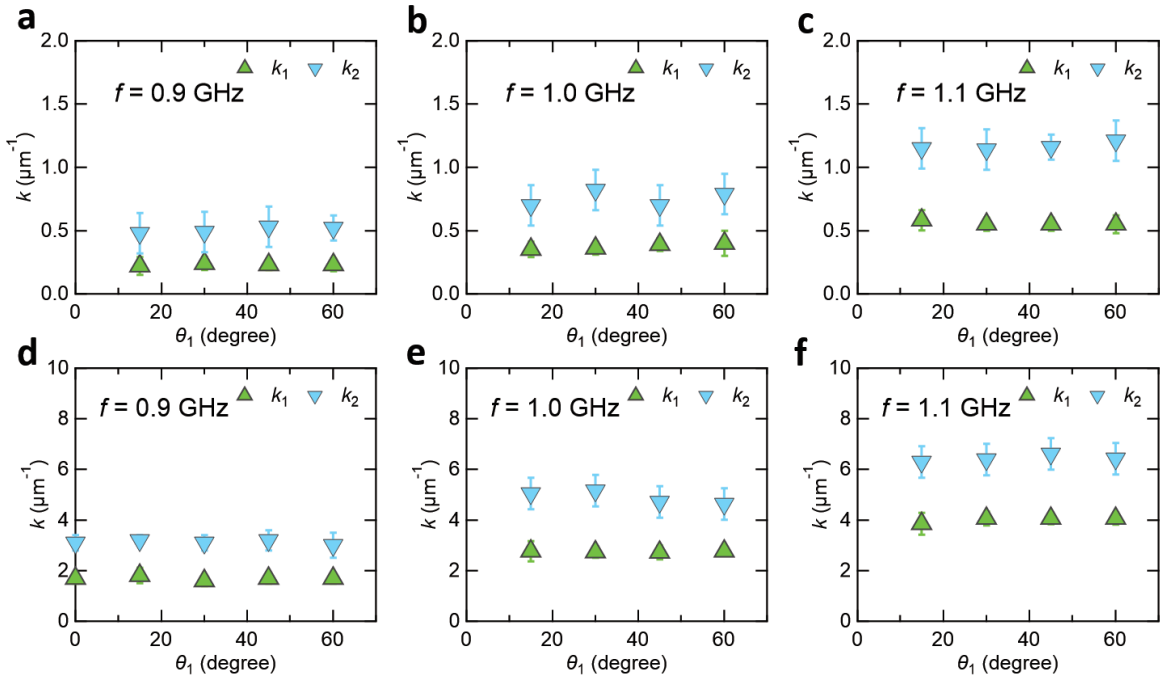

Fig.2 Incident angle dependent k_1 and k_2 in sample A (a,b,c) and sample B (d,e,f). The SWs are excited at three different resonant frequencies; 0.9 GHz (a,d),1.0 GHz (b,d), and 1.1 GHz (c,f). The green markers show k_1 and the blue markers show k_2.

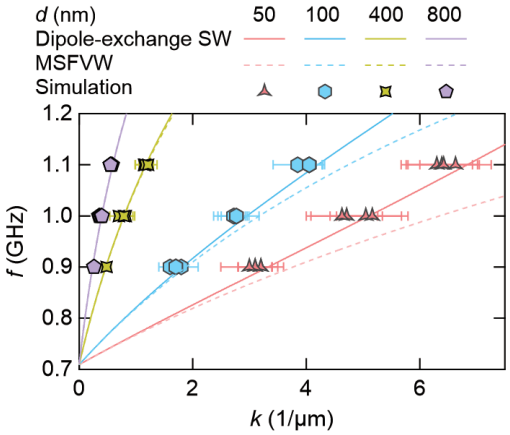

Fig.3 The resonant frequency as a function of wavenumber. Dispersion relation of DEFVW and MSFVW are respectively described by the solid and broken lines and the simulation results are plotted by the markers. Purple and green markers represent the SWs in the film of $d = 800$ nm and 400 nm, referring to the data of k_1 and k_2 in sample A, respectively. The blue and red markers represent the SWs in the film of $d = 100$ nm and 50 nm , referring to the data of k_1 and k_2 in sample B, respectively.

Fig. 3 shows the resonant frequency as a function of wavenumber. Symbols show the results by the micromagnetic simulation, and the calculation results by Eq. (1) and Eq. (2) are shown by broken lines and solid lines, respectively. While the simulation results in the regions of 400 and 800 nm thicknesses (sample A) are well reproduced by Eq. (2), those in the regions of 50 and 100 nm thicknesses (sample B) show deviation from Eq. (2) and can be explained by Eq. (1), indicating that not only the dipole interaction but also the exchange interaction should be taken into account to describe the refraction of spin waves with high wavenumbers.

Figs. 4(a) and 4(b) show the relation between the incident angle θ_1 and the refraction angle θ_2 observed in the samples A and B, respectively. The refraction angle is independent of the resonant frequency in the sample A. This is due to the specific nature of MSFVW. According to Eq. (2) for MSFVW, the wavenumber varies by keeping kd constant, resulting in the special conditon of $k_1/k_2 = d_2/d_1$. Therefore, Snell's law, $\sin\theta_1/\sin\theta_2 = k_2/k_1$, is given solely by the thickness ratio of two regions. On the other hand, in the case of the dipole-exchange forward volume wave (DEFVW) described by Eq. (1), the ratio k_2/k_1 depends not only on the thickness ratio but also on the frequency. Note that similar effect is also well known in optics as the chromatic aberration due to the dependence of refractive index on wavelength of light. The lines in Figs. 4(a) and 4(b) show the calculation results of Snell's law based on Eq. (1) and on Eq. (2), respectively, and the simulation results well reproduce the calculation results, confirming that the refraction of SWs follows the Snell's law in optics with the chromatic aberration effect.

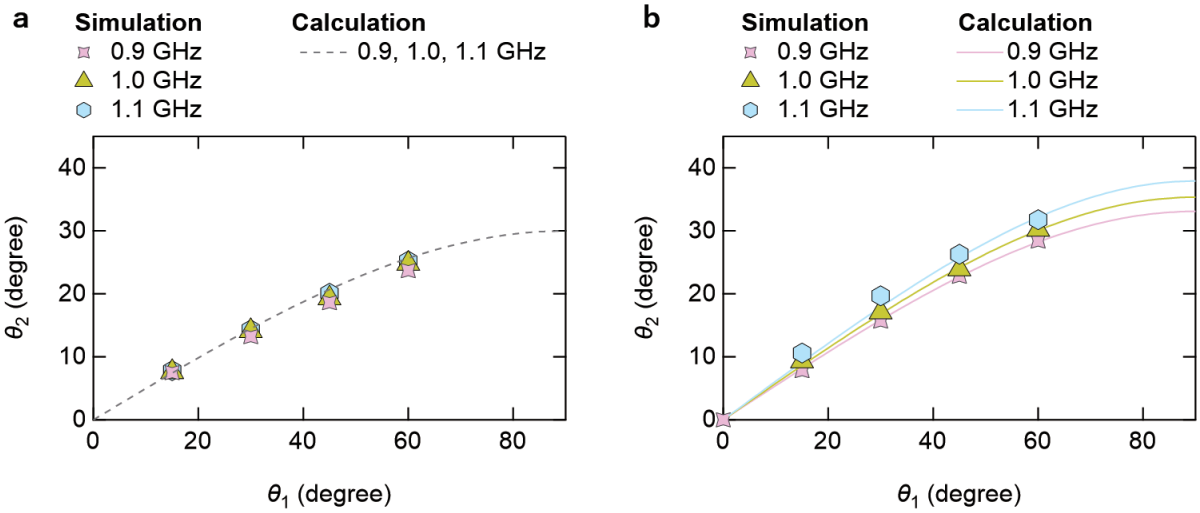

Fig.4 Refraction angle versus incident angle of the SWs propagating (a) in sample A and (b) in sample B. In both figures, the pink, green, and blue markers correspond to the simulation results of $f = 0.9$, 1.0, and 1.1 GHz, respectively. (a) Snell's law of MSFVW is expressed by the black dashed line. (b) The frequency dependent Snell's law of 0.9, 1.0, and 1.1 GHz are shown by the pink, green, and blue solid lines, respectively.

In summary, we performed the micromagnetic simulations to investigate the refraction of SWs across the thickness step in magnetic thin films with out-of-plane magnetization. It was confirmed that the SWs propagate isotropically and the Snell's law in optics can be applied in the present system, leading to the simple design of magnonic devices. It was also found that while the refraction angle is independent of the resonant frequency in MSFVW it depends on the resonant frequency in the case of DEFVW, suggesting that the chromatic aberration effect should be taken into account in designing magnonic devices using spin waves with high wavenumbers.

Acknowledgements We gratefully acknowledge funding of JSPS KAKENHI Grant Numbers 15H05702, 18J22219, Collaborative Research Program of the Institute for Chemical Research, Kyoto University, and the Cooperative Research Project Program of the Research Institute of Electrical Communication, Tohoku University.

References

1) R. L. Stamps, S. Breitkreutz, J. Åkerman, A. V. Chumak, Y. Otani, G. E. W. Bauer, J. –U. Thiele, M. Bowen, S. A. Majetich, and M. Kläui: *Journal of Physics D: Applied Physics*, **47**(33), 333001 (2014).
2) J. M. Owens, J. H. Collins, and R. L. Carter, Circuits; *Systems and signal processing*, **4**(1-2), 317-334 (1985).
3) J. D. Adam: *Proceedings of the IEEE*, **76**(2), 159-170 (1988).
4) A. V. Chumak, V. I. Vasyuchka, A. A. Serga, and B. Hillebrands: *Nat. Phys.*, **11**, 453 (2015).
5) P. Gruszecki, Yu. S. Dadoenkova, N. N. Dadoenkova, I. L. Lyubchanskii, J. Romero-Vivas, K. Y. Guslienko, and M. Krawczyk: *Phys. Rev. B*, **92**, 054427 (2015).
6) P. Gruszecki, J. Romero-Vivas, Yu. S. Dadoenkova, N. N. Dadoenkova, I. L. Lyubchanskii, and M. Krawczyk: *Appl. Phys. Lett.*, **105**, 242406 (2014).
7) K. Yasumoto and Y. Ōishi: *J. Appl. Phys.*, **54**, 2170 (1983).
8) R. Gieniusz, V. D. Bessonov, U. Guzowska, A. I. Stognii, and A. Maziewski: *Appl. Phys. Lett.*, **104**, 082412 (2014).
9) Y. I. Gorobets and S. A. Reshetnyak, *Technical Physics*, **43**(2), 188-191 (1998).
10) B. A. Kalinikos and A. N. Slavin: *J. Phys. C: Solid State Phys.*, **19**, 7013 (1986).
11) J. –N. Toedt, M. Mundkowski, D. Heitmann, S. Mendach, and W. Hansen: *Sci. Rep.*, **6**, 33169 (2016).
12) H. Hata, T. Moriyama, K. Tanabe, K. Kobayashi, R. Matsumoto, S. Murakami, J. –I. Ohe, D. Chiba, T. Ono: *J. Magn. Soc. Jpn.*, **39**, 151 (2015).
13) J. Stigloher, M. Decker, H. S. Körner, K. Tanabe, T. Moriyama, T. Taniguchi, H. Hata, M. Madami, G. Gubbiotti, K. Kobayashi, T. Ono, and C. H. Back: *Phys. Rev. Lett.*, **117**, 037204 (2016).
14) D. –E. Jeong, D. –S. Han, and S. –K. Kim: *Spin*, **1**, 27-31 (2011).
15) G. Csaba, A. Papp, and W. Porod: *J. Appl. Phys.*, **115**, 17C741 (2014).
16) J. Stigloher, T. Taniguchi, M. Madami, M. Decker, H. S. Körner, T. Moriyama, G. Gubbiotti, T. Ono, and C. H. Back: *Appl. Phys. Express*, **11**, 053002 (2018).
17) K. Tanabe, R. Matsumoto, J. –I. Ohe, S. Murakami, T. Moriyama, D. Chiba, K. Kobayashi, and T. Ono: *Appl. Phys. Express*, **7**, 053001 (2014).
18) S. -K. Kim, S. Choi, K. –S. Lee, D. –S. Han, D. –E. Jung, and Y. –S. Choi: *Appl. Phys. Lett.*, **92**, 212501 (2008).
19) A. Vansteenkiste, J. Leliaert, M. Dvornik, M. Helsen, F. Garcia-Sanchez, and B. Van Waeyenberge: *AIP Advances*, **4**, 107133 (2014).
20) A. S. KindyakV., A. KolosovL., and N. Makutina: *j. Mater. Sci.: Mater. Electron.*, **6**, 25-27 (1995).
21) A. V. Chumak, A. A. Serga, and B. Hillebrands: *Nat. Commun.*, 5, 4700 (2014).
22) M. H. Seavey, Jr., and P. E. Tannenwald: *Phys. Rev. Lett.*, **1**, 168 (1958).

Received Aug. 27, 2020; Revised Sep. 18, 2020; Accepted Sep. 23, 2020

J. Magn. Soc. Jpn., **44**, 137-144 (2020)

<Review>

Spin Hall effect in topological insulators

Pham Nam Hai[1,2]

[1] Department of Electrical and Electronic Engineering, Tokyo Institute of Technology,
2-12-1 Ookayama, Meguro, Tokyo 152-8550, Japan

[2] Center for Spintronics Research Network (CSRN), The University of Tokyo,
7-3-1 Hongo, Bunkyo, Tokyo 113-8656, Japan

The giant spin Hall effect (SHE) in topological insulators (TIs) is very attractive for applications to various spintronic devices, notably spin-orbit torque magnetoresistive random-access memory (SOT-MRAM). In this paper, we review the recent progress on the giant SHE in TIs, with emphasis on the role of topological surface states. We discuss current challenges and future prospects for TIs as a realistic material in SOT-MRAM.

Key words: spin Hall effect, topological insulator, spin-orbit torque, MRAM

1. Introduction

The spin Hall effect (SHE)[1,2] in non-magnetic materials with strong spin-orbit coupling has recently attracted great interest for its possible applications to various spintronic devices, most notably spin-orbit torque (SOT) magnetoresistive random-access memory (MRAM). In the SHE, a perpendicular pure spin current density J_s can be generated by an in-plane charge current density J_e in a non-magnetic layer, whose charge-to-spin conversion efficiency is characterized by the spin Hall angle $\theta_{SH} = (2e/\hbar)J_s/J_e$. This pure spin current can be injected into the free magnetic layer of a magnetic tunnel junction (MTJ), and it consequently exerts a spin torque on the layer for magnetization switching. The relationship between the injected spin current I_s and the charge current I_e in the non-magnetic layer is then given by $I_s = (\hbar/2e)(L/t)\theta_{SH}I_e$, where L is the length of the magnetic layer, and t the thickness of the non-magnetic layer. Because the factor $(L/t)\theta_{SH}$ can be much larger than unity, i.e. $I_s/(\hbar/2) >> I_e/e$, the SHE can be used as an effective way of generating a spin current, meaning that a small writing current can be used for magnetization switching. Furthermore, since there is no charge current flowing into the magnetic layer, damage to MTJs can be suppressed. Finally, since the spin-polarization direction of the pure spin current generated by the SHE is perpendicular to the magnetization direction of the free magnetic layer with perpendicular magnetic anisotropy (PMA), the anti-dampling-like spin torque is maximized and the magnetization can be switched very fast (< ns).[3] Motivated by these prospects, there have been intensive efforts put into the research and development of SOT-MRAM. In particular, very fast switching with low voltage and no in-plane bias field has been demonstrated in SOT-MRAM arrays deposited on 300 mm Si wafers, underlying the feasibility of SOT-MRAM.[4]

Despite these recent developments, the writing current density in SOT-MRAM is still as large as 10^8 Acm^{-2}, which is too high for implementing SOT-MRAM with Si driving transistors. This is because the heavy metals used for the spin Hall layer in SOT-MRAM, such as Ta, Pt or W, have a limited spin Hall angle. The maximum θ_{SH}, ~0.4, is obtained with W.[5] Even if taking into account the L/t factor, the driving current in SOT-MRAM is still one order of magnitude larger than that of the conventional spin-transfer torque MRAM. To solve this bottle neck, it is essential to find new materials with spin Hall angles at least one order of magnitude larger than that of heavy metals, which requires $\theta_{SH} > 1$. Since the extrinsic mechanism of SHE, i.e. side-jump or skew scattering, unlikely yields such a giant θ_{SH}, we can rely only on its intrinsic mechanism,[6] which originates from Berry-phase curvature in the momentum space and is an intrinsic quantum-mechanical property of the band structure.[7] Because Berry-phase curvature has a singularity at Dirac points, we can expect a very large θ_{SH} in materials with Dirac-like dispersion. Topological insulators (TIs) are promising since they have metallic surface states with Dirac-point-like dispersion. In fact, very large θ_{SH}, usually higher than 1, have been routinely observed in many TIs, which is a breakthrough for SOT-MRAM. In this paper, we will briefly introduce some fundamental properties of TIs. Then, we will review recent studies on the giant SHE in TIs, with emphasis on the role of topological surface states. Finally, we will discuss the current challenges and future prospects for TIs as a realistic material in SOT-MRAM.

2. Brief history and fundamental properties of topological insulators

TIs are quantum materials having insulating bulk states and metallic surface states with spin-momentum locking, as shown in Fig. 1. TIs have had roots in research on the quantum Hall effect since the early 1980s. When two-dimensional electron gas at the interface of a semiconductor heterostructure is subjected to low temperatures and strong magnetic fields, its energies are quantized to multiple Landau levels. If the Fermi level lies in between those Landau levels, the charge conduction inside the sample is suppressed, and the inside of the sample becomes insulating with only one-dimensional conduction at the

edges of the sample. Thus, electron gas undergoing the quantum Hall effect can be considered as a two-dimensional TI with one-dimensional edge states. It was later found that the quantum Hall effect originates from the non-trivial topology of the two-dimensional electron wavefunctions under strong magnetic fields.[8] This further led to the prediction of a novel quantum Hall effect without Landau levels (quantum anomalous Hall effect) based purely on topology arguments by Haldane in 1988.[9] Then, in 2006, a two-dimensional TI with spin-polarized edge states was predicted in a heterostructure consisting of a HgTe quantum well sandwiched by two (HgCd)Te barriers.[10] For this heterostructure, spin-polarized edge states were predicted even without a magnetic field (quantum spin Hall effect), and immediately confirmed.[11] These theoretical and experimental achievements opened the dawn of TI research. Theories on quantum spin Hall states were further studied for the two-dimensional surface states of three-dimensional TI materials,[12] and BiSb (Sb composition of 7–22%) was proposed as a three-dimensional TI.[13] The topological surface states of BiSb and their spin-momentum locking were confirmed by using angle-resolved photoemission spectroscopy,[14,15] making it the first experimentally confirmed three-dimensional TI. This sparked a gold rush of both theoretical and experimental searches for new three-dimensional TI materials. Among them, Bi-based chalcogenides, such as Bi_2Se_3, Bi_2Te_3, and $(BiSb)_2Te_3$, are the most studied for their electronic properties and possible device applications because they have a large band gap and a single surface state with simple Dirac-like band dispersion and because their thin films can be easily grown on various substrates using the molecular beam epitaxy (MBE) technique.[16–20] Notably, Cr-doped magnetic TI $(CrBiSb)_2Te_3$ with PMA was synthesized, in which the quantum anomalous Hall effect was finally confirmed.[21]

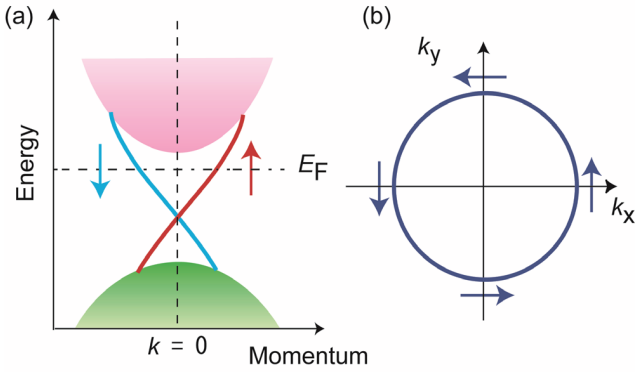

Fig. 1. (a) Typical band structure of TI, having insulating bulk and Dirac-like metallic surface states. (b) Spin-momentum locking of electrons on topological surfaces.

From this brief history, we can see that TIs inherit many properties of quantum Hall states and thereby have been the object of many studies on low-temperature physics such as the quantum spin Hall effect or quantum anomalous Hall effect. At the same time, TIs have many different characteristics from quantum Hall states that make them attractive for room-temperature spintronic applications. One feature is that the existence of one(two)-dimensional edge(surface) states of TIs is ensured by the non-trivial topology of their band structure and can emerge without the application of large external magnetic fields. If the band gap energy is much larger than the thermal energy at room temperature and the Fermi level is inside the band gap, the edge(surface) states can be electrically accessed even at room temperature. Another is that the surface states have Dirac-like band dispersion, which promises a large intrinsic SHE. Yet another feature is the unique spin-momentum locking feature of the surface states, which prioritizes pure spin current generation in the direction perpendicular to the film plane. All of these features are very promising for applications to spintronics, especially their expected giant SHE.

3. Spin Hall effect in Bi_2Se_3

Bi_2Se_3 is a TI with a large band gap of about 300 meV and has thus become one of the most studied TIs. As a result, the SHE in TIs was first evaluated in Bi_2Se_3. A.R. Mellnik *et al.* cleaned the surface of a MBE-grown Bi_2Se_3 layer and deposited NiFe on top of it. They then used the spin torque ferromagnetic resonance (ST-FMR) technique to determine the spin Hall angle.[22] The obtained θ_{SH} = 2–3.5 was larger than that of heavy metals by one order of magnitude. This work immediately generated great interest in the SHE of TIs. Nevertheless, studies on the SHE in Bi_2Se_3 face a big problem. Since Bi_2Se_3 is a V-VI group compound, strict control of the stoichiometry is required to obtain the insulating bulk. In reality, due to the existence of anti-site Se or anti-site Bi defects during MBE growth, there are always extrinsic electrons or holes that shift the Fermi level to either the conduction band or the valence band, making the bulk of Bi_2Se_3 a degenerated semiconductor. Therefore, there can exist parallel conduction in the bulk and on the surfaces of Bi_2Se_3. In such a situation, it becomes impossible to separate the electric currents flowing in the bulk and on the surfaces of Bi_2Se_3. The ratio between the surface current and the bulk current may vary from sample to sample, depending on the growth condition and the thickness of the Bi_2Se_3 thin film. Consequently, there has been a broad distribution of reported θ_{SH} values for Bi_2Se_3, making it difficult to draw a clear conclusion about the origin of the giant SHE in Bi_2Se_3, i.e. whether the observed giant spin Hall angle is real and originates from the surface states or not. For example, Y. Wang *et*

al. used the same ST-FMR technique to measure the spin Hall angle in Bi_2Se_3/CoFeB bilayers, but obtained only θ_{SH} = 0.047 (room temperature) ~ 0.42 (50 K).[23] Meanwhile, the same group reported θ_{SH} = 1–1.75 and successfully realized room-temperature SOT magnetization switching in Bi_2Se_3/NiFe bilayers with a current density as low as 6×10^5 Acm^{-2}.[24]

4. Spin Hall effect in $(BiSb)_2Te_3$

$(BiSb)_2Te_3$ is a ternary TI that can avoid the bulk current problem in Bi_2Se_3. Since Bi_2Te_3 tends to be n-type while Sb_2Te_3 tends to be p-type, it is possible to prepare alloy $(BiSb)_2Te_3$ thin films with insulating bulk by adjusting the Sb composition (88–96%).[25] The spin Hal angle of $(BiSb)_2Te_3$ was first evaluated in $(Bi_{0.5}Sb_{0.5})_2Te_3/(Cr_{0.08}Bi_{0.54}Sb_{0.38})_2Te_3$ bilayers.[26] Because $(Cr_{0.08}Bi_{0.54}Sb_{0.38})_2Te_3$ is a diluted magnetic TI with a low Curie temperature, the experiment was performed at 1.9 K. SOT magnetization switching was realized at a very low current density of 8.9×10^4 Acm^{-2}. The spin Hall angle was investigated with second harmonic Hall measurements. However, the obtained θ_{SH} = 140–425 value may have been significantly overestimated due to an artifact from the asymmetric magnon scattering on the surfaces of $(Cr_{0.08}Bi_{0.54}Sb_{0.38})_2Te_3$.[27] The corrected value was obtained later in $(BiSb)_2Te_3$/Ti/CoFeB junctions, which yielded θ_{SH} = 2.5 at room temperature.

5. Room temperature SOT magnetization switching by topological insulators

Room temperature SOT magnetization switching and its advantage compared with heavy metals was first demonstrated by J. Han *et al.* using Bi_2Se_3, $(BiSb)_2Te_3$, Ta, and Pt/CoTb bilayers.[28] Figures 2(a) and 2(b) show the SOT magnetization switching loops of the Bi_2Se_3/CoTb (4.6 nm) bilayer, while Figs. 2(c) and 2(d) show that of the reference Pt/CoTb (2 nm) and Ta/CoTb (2 nm) bilayer, respectively. The threshold switching current density in the Bi_2Se_3/CoTb (4.6 nm) bilayer was 3×10^6 Acm^{-2}, which was much smaller than of Pt/CoTb (2 nm) (40×10^6 Acm^{-2}) and Ta/CoTb (2 nm) (10×10^6 Acm^{-2}).

Figure 3(a) shows the effective spin Hall angle of $(BiSb)_2Te_3$, Bi_2Se_3, Pt, and Ta in junctions with CoTb measured by the loop shift method. The effective spin Hall angles of $(BiSb)_2Te_3$, Bi_2Se_3, Pt and Ta were 0.4, 0.16, 0.017, and –0.031, respectively. These values were smaller than their intrinsic values, which is explained by the small spin transmissivity of CoTb. Nevertheless, the effective spin Hall angles of $(BiSb)_2Te_3$ and Bi_2Se_3 are clearly larger than those of Pt and Ta. Figure 3(b) compares the power consumption of SOT switching using $(BiSb)_2Te_3$, Bi_2Se_3, Pt, and Ta, which confirmed the advantage of TIs.

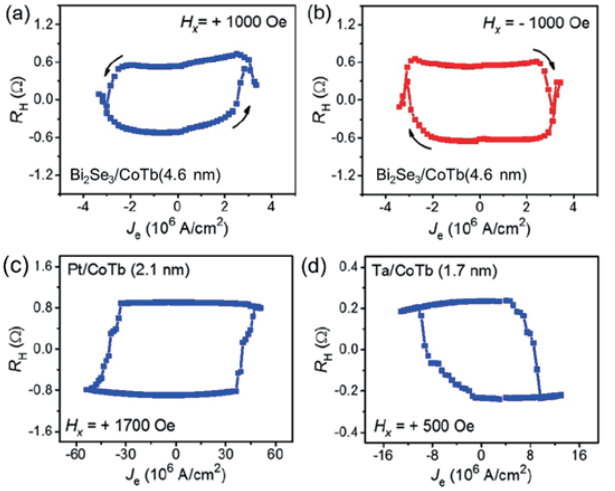

Fig. 2. (a)(b) Room temperature SOT switching loops of Bi_2Se_3/CoTb bilayer, measured under bias field of ±1000 Oe, respectively. (c)(d) SOT switching loop of reference Pt/CoTb and Ta/CoTb bilayer, respectively. Here, J_e is charge current density inside spin Hall materials. Reprinted with permission from Ref. 28). Copyright (2017) by American Physical Society.

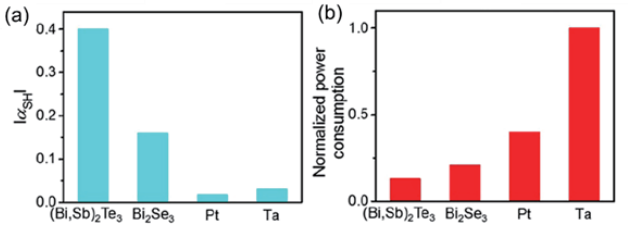

Fig. 3. (a) Effective spin Hall angles of $(BiSb)_2Te_3$, Bi_2Se_3, Pt, and Ta measured in junctions with CoTb. (b) Normalized power consumption (with Ta set to be unity) for SOT switching using $(BiSb)_2Te_3$, Bi_2Se_3, Pt, and Ta. Reprinted with permission from Ref. 28). Copyright (2017) by American Physical Society.

6. Role of topological surface states

Although giant spin Hall angles and low SOT switching current densities have been confirmed in various TI/ferromagnet bilayers, the origin of the giant SHE in TIs is still not clear due to the fact that the current may flow on both the surfaces and in the bulk of TIs. To definitely determine the origin of the giant SHE in TIs, H. Wu *et al.* investigated the SHE in $(Bi_{1-x}Sb_x)_2Te_3$ thin films with varying Sb compositions.[29] As shown in Fig. 4(a), the Fermi level of $(Bi_{1-x}Sb_x)_2Te_3$ can be tuned by changing the Sb composition. When the Sb composition is about 93%, the Fermi level approaches the Dirac point. Figure 4(b) shows the sheet carrier density and the resistivity of $(Bi_{1-x}Sb_x)_2Te_3$ as a function of Sb composition. Near the Dirac point, the electron sheet density decreases and the resistivity reaches the maximum at x = 93%, which

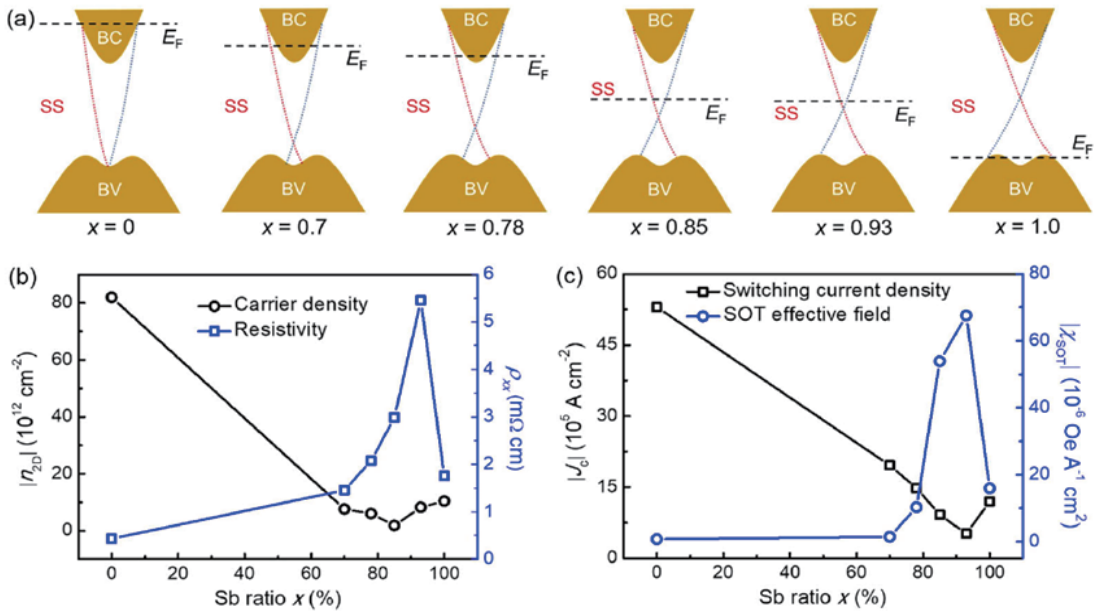

Fig. 4. (a) Schematic of Fermi level positions for different Sb ratios (x = 0, 0.7, 0.78, 0.85, 0.93, 1.0) of $(Bi_{1-x}Sb_x)_2Te_3$. (b) Sheet carrier density $|n_{2D}|$ and resistivity ρ_{xx} as function of Sb composition in $(Bi_{1-x}Sb_x)_2Te_3$. (c) Switching current density $|J_c|$ and SOT-induced effective field $|\chi_{SOT}|$ as function of Sb composition. Reprinted with permission from Ref. 29). Copyright (2019) by American Physical Society.

indicates that the Fermi level is inside the band gap and approaches the Dirac point. Figure 4(c) shows the threshold switching current density and the SOT-induced effective field as a function of Sb composition in $(Bi_{1-x}Sb_x)_2Te_3$/Ti/CoFeB junctions. Near the Dirac point, the switching current density J_c is at the minimum, and the SOT-induced effective field is maximized. This unambiguously demonstrates the surface state origin of the giant SHE. The J_c of the $(Bi_{0.07}Sb_{0.93})_2Te_3$/Ti/CoFeB junction is reduced to 5.2 × 10^5 Acm^{-2}, which is one to two orders of magnitude smaller than that of the reference Pt,Ta,W/Ti/CoFeB junctions. Furthermore, θ_{SH} = 2.5 was obtained for the $(Bi_{0.07}Sb_{0.93})_2Te_3$/Ti/CoFeB junction from second harmonic Hall measurements.

7. High electrical conductivity and giant spin Hall effect in BiSb

One disadvantage of using TIs as the spin Hall material in SOT-MRAM is their low electrical conductivity σ of ~10^4 Ω^{-1}m^{-1}. For example, the σ of $(Bi_{0.07}Sb_{0.93})_2Te_3$ discussed in the previous section is only 1.8 × 10^4 Ω^{-1}m^{-1}, which is significantly smaller than the 6 × 10^5 Ω^{-1}m^{-1} of CoFeB. Therefore, in the junctions of TI/metallic ferromagnets, most of the current will be shunted by the ferromagnetic layer and does not contribute to the generation of a pure spin current. For example, in a typical $(Bi_{0.07}Sb_{0.93})_2Te_3$ (six quintuple layers)/CoFeB (1.5 nm) bilayer, 87% of the current will flow into the CoFeB layer. Therefore, finding a TI material with both high conductivity and a giant spin Hall effect is essential. Thus, we have been concentrating on BiSb.[30] Although BiSb is the first experimentally confirmed three-dimensional TI (Sb of 7–22%), it has a small bulk band gap of ~20 meV and complex surface states. Therefore, not much attention has been paid to BiSb since the discovery of Bi_2Se_3 and related compounds with a much larger band gap of ~300 meV and much simpler surface states. However, as a pure spin current source for SOT-MRAM, BiSb is very attractive because it has multiple surface states and high mobility as evidenced by the high bulk electrical conductivity of 4~6.4 × 10^5 Ω^{-1}m^{-1}. Furthermore, because Bi and Sb are in the same V-group, deviation of the composition or existence of anti-site defects does not result in any donors/acceptors that would generate free carriers and shift the Fermi level to the conduction band or to the valence band as in the case of Bi_2Se_3. As a result, the Fermi level of BiSb is always in the band gap, making it easier to investigate the origin of the SHE. Motivated by these promising prospects, we grew and characterized $Bi_{1-x}Sb_x$ thin films on semi-insulating GaAs(111)A substrates by MBE, with various Sb concentration ranging from 0 to 100%. By optimizing the growth condition, we were able to grow single crystalline $Bi_{1-x}Sb_x$ thin films on GaAs(111)A substrates, despite the large and changing lattice mismatch between $Bi_{1-x}Sb_x$ and GaAs(111) as the Sb concentration changes. For thick enough thin films, their conductivity approached those of bulk values, indicating that the crystal quality was high. From the temperature dependence of the electrical conductivity, we confirmed the existence of the metallic surface states of $Bi_{1-x}Sb_x$.[31]

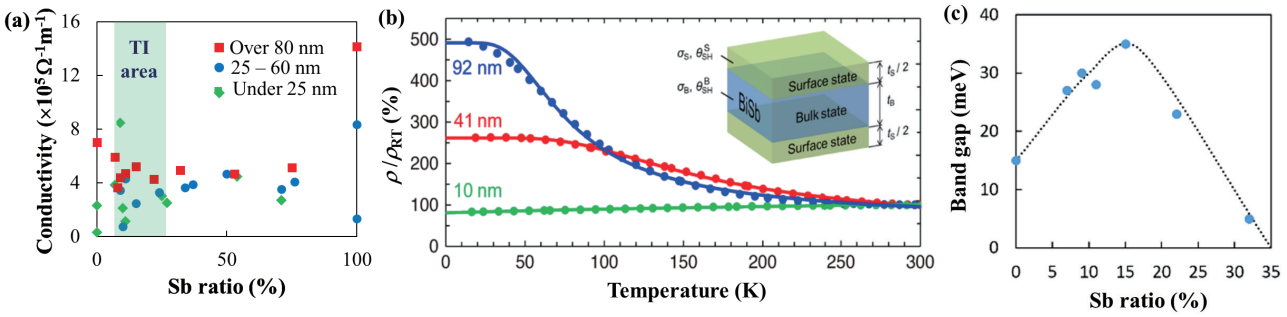

Fig. 5. (a) Room-temperature electrical conductivity of various $Bi_{1-x}Sb_x$ thin films with different Sb concentrations and thicknesses. (b) Temperature dependence of resistivity (normalized by value at room temperature) in $Bi_{0.89}Sb_{0.11}$ thin films with thicknesses of 10, 41, and 92 nm. Dots and solid lines show experimental data and fitting to parallel conduction model of BiSb (inset). (c) Band gap of $Bi_{1-x}Sb_x$ thin films with thicknesses around 90 nm, obtained by fitting their experimental temperature dependence of resistivity to parallel conduction model.[30,31]

Figure 5(a) shows the electrical conductivity σ of various $Bi_{1-x}Sb_x$ samples with different thickness and Sb concentrations x. We found that $Bi_{1-x}Sb_x$ thin films show electrical conductivity higher than $1 \times 10^5\ \Omega^{-1}m^{-1}$ with an average of $2.5 \times 10^5\ \Omega^{-1}m^{-1}$, which is higher than other Bi-based chalcogenides by one order of magnitude. Figure 5(b) shows the temperature dependence of the normalized resistivity of $Bi_{0.89}Sb_{0.11}$ thin films with thicknesses of 10 nm, 41 nm, and 92 nm. For the 92 nm-thick thin film, the resistivity exponentially increased as the temperature decreased as expected for an intrinsic semiconductor, but it approached a constant value at low temperatures. This behavior can be explained by the parallel conduction model for this sample. At high temperatures, bulk conduction occurs due to thermally excited intrinsic carriers in the conduction band and valence band. As the temperature decreases, the bulk conduction is quenched, and the surface conduction becomes dominant at low temperatures. As the thickness reduced to 41 nm, the surface state contribution began to rise significantly. Finally, the 10-nm-thick sample showed metallic behavior over the wide range of temperature. This indicates that surface conduction was dominant for the thinnest sample. Another important feature of BiSb is the quantum confinement effect that adds an extra band gap energy to the intrinsic bulk band gap. Figure 5(c) shows the band gap of various $Bi_{1-x}Sb_x$ thin films with thicknesses around 90 nm, obtained by fitting the experimental temperature dependence of resistivity to the parallel conduction model. Although the bulk $Bi_{1-x}Sb_x$ only has a band gap for x = 7–22% with a maximum value of about 20 meV at x = 15%, the actual band gap is enhanced by the quantum confinement effect, which is effective at small thicknesses. Furthermore, the band gap exists not only inside the bulk TI regions ($0.07 \le x \le 0.22$) but also outside of the TI region ($x < 0.07$ and $0.22 < x < 0.35$), which is also due to the quantum confinement effect, as can be seen in Fig. 5(c). For the 10-nm-thick BiSb (x = 15%), the band gap increased to 200 meV, which is large enough so that most of the current flowed on the surfaces. The strong quantum confinement effect reflects the high crystal quality of BiSb thin films.

To evaluate the SHE in BiSb, we prepared $Mn_{0.45}Ga_{0.55}$ (3 nm)/$Bi_{0.9}Sb_{0.1}$ (10 nm) bilayers grown on GaAs(001) substrates. Because MnGa on GaAs(001) has a cubic crystal structure, BiSb grown on top of MnGa has a pseudo-cubic (012) orientation. MnGa has a very large perpendicular anisotropy field of 40–50 kOe. However, at the Mn concentration of 45%, the magnetization of MnGa is not perfectly perpendicular, but tilts toward the in-plane direction.[32] The spin Hall angle was measured by the loop-shift technique with the experimental setup shown in Fig. 6(a). The pure spin current injected from BiSb to MnGa generated an effective anti-damping-like SOT field H_{SO} that can either increase or decrease the coercive force of MnGa, depending on the current direction. Figure 6(b) shows the perpendicular hysteresis loops of MnGa measured under different current densities and polarities. Figure 6(c) plots the coercive force of MnGa and its change, which is equal to the effective SOT field, as a function of the current density inside the BiSb layer. This data indicates that the effective SOT field was as large as 2.3 kOe per (10^6 Acm^{-2}), which yielded θ_{SH} = 52 for the BiSb(012) orientation.[33] The giant spin Hall angle for the BiSb(012) surfaces can be understood by the fact that there are multiple Dirac points for the BiSb(012) surface states, compared with only one Dirac point for the (001) surface states.[34]

Figure 7 shows SOT magnetization switching loops for a $Mn_{0.45}Ga_{0.55}$ (3 nm)/$Bi_{0.9}Sb_{0.1}$ (5 nm) bilayer. The threshold switching current density is only 1.5×10^6 Acm^{-2}, which is smaller than that of MnGa/Pt,Ta,IrMn bilayers by two orders of magnitude.[35-37]

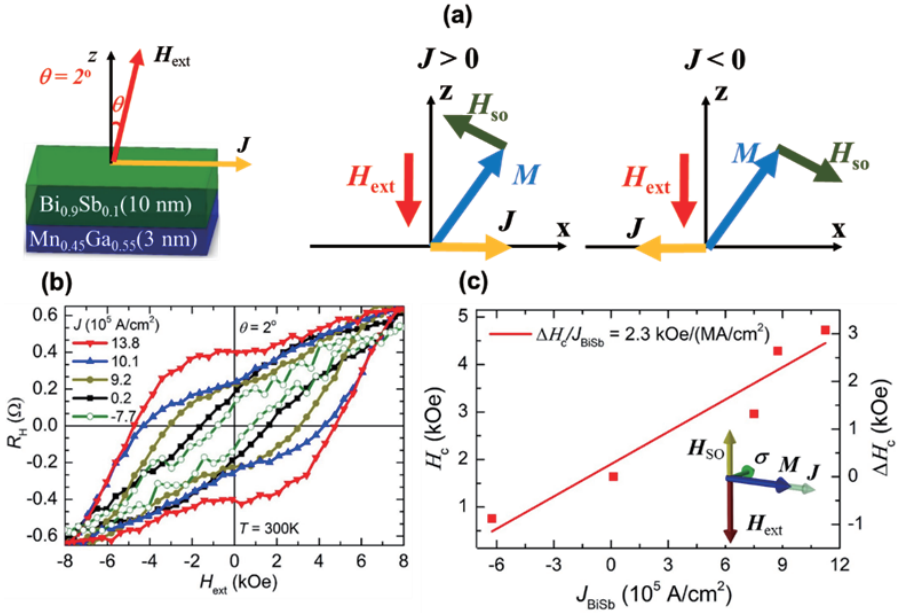

Fig. 6. (a) Experimental setup for measuring SHE in $Bi_{0.9}Sb_{0.1}$ (10 nm) / $Mn_{0.45}Ga_{0.55}$ (3 nm) bilayer. (b) Hall resistance of 100-μm × 50-μm Hall bar device of $Bi_{0.9}Sb_{0.1}$ (10 nm) / $Mn_{0.45}Ga_{0.55}$ (3 nm) bilayer under slightly tilting perpendicular magnetic field H_{ext} (θ = 2°), measured with various current densities $J = -7.7 - 13.8 \times 10^5$ Acm^{-2} at room temperature. (c) Coercive force H_c of MnGa and its change ΔH_c as function of current density J_{BiSb} in BiSb layer. Inset shows perpendicular effective SOT magnetic field H_{so} acting on magnetization vector M at $H_{ext} = -H_c$ (coercive force) in macrospin picture.[30),33)]

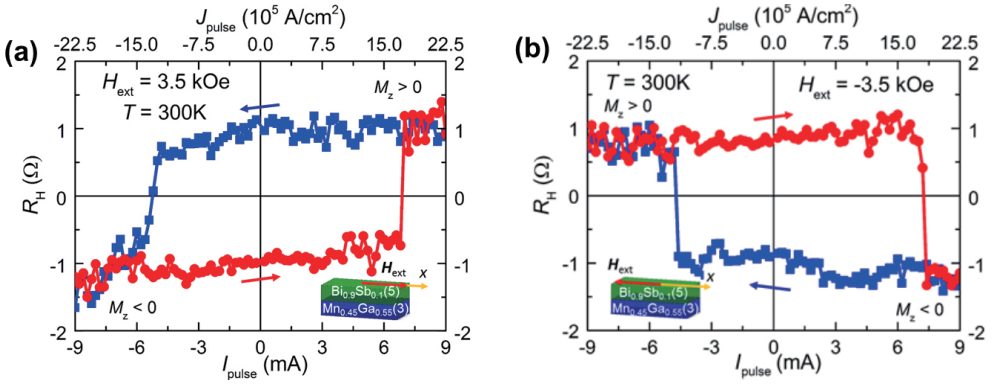

Fig 7. Room-temperature SOT magnetization switching in $Bi_{0.9}Sb_{0.1}$ (5 nm)/$Mn_{0.45}Ga_{0.55}$ (3 nm) bilayer. (a) (b) Hall resistance of 100-μm × 50-μm Hall bar of bilayer under 100-ms pulse currents and in-plane magnetic field of +3.5 kOe and –3.5 kOe, respectively.[33)]

8. Current challenges and future prospects

Figure 8 shows the expected writing current and writing energy of a realistic SOT-MRAM device using various type of materials for the pure spin current source, including heavy metals, two-dimensional materials, and topological insulators.[38)] It can be seen that our MBE-grown BiSb outperformed all other materials by several orders of magnitude, because BiSb shows not only high electrical conductivity but also a giant spin Hall angle. However, most of the TIs thin films studied so far, including BiSb, were epitaxially grown on dedicated III-V semiconductor substrates by the MBE technique, which is not suitable for mass-production. Therefore, it is essential to investigate the performance of non-epitaxial TIs thin films deposited on silicon substrates with an industry-friendly technique, such as sputtering deposition. Recently, there was an attempt to investigate the performance of sputtered non-epitaxial Bi_xSe_{1-x} TI thin films by Mahendra DC *et al.*,[39)] who found a promisingly large θ_{SH} = 8.7–18.6 but very low σ = 7.8 × 10^3 Ω^{-1}m^{-1}. On the other hand, we have demonstrated that it is possible to deposit BiSb thin films on sapphire substrates by sputtering deposition with a high crystal quality and high electrical conductivity approaching those of MBE-grown thin films.[40)] Furthermore, we found that even non-epitaxial BiSb thin films deposited on Si substrates by MBE or

sputtering deposition could show a high spin Hall performance.[41] Further work is needed to demonstrate BiSb thin films with a high crystal quality and optimized spin Hall performance on Si substrates with sputtering deposition for ultralow power SOT-MRAM.

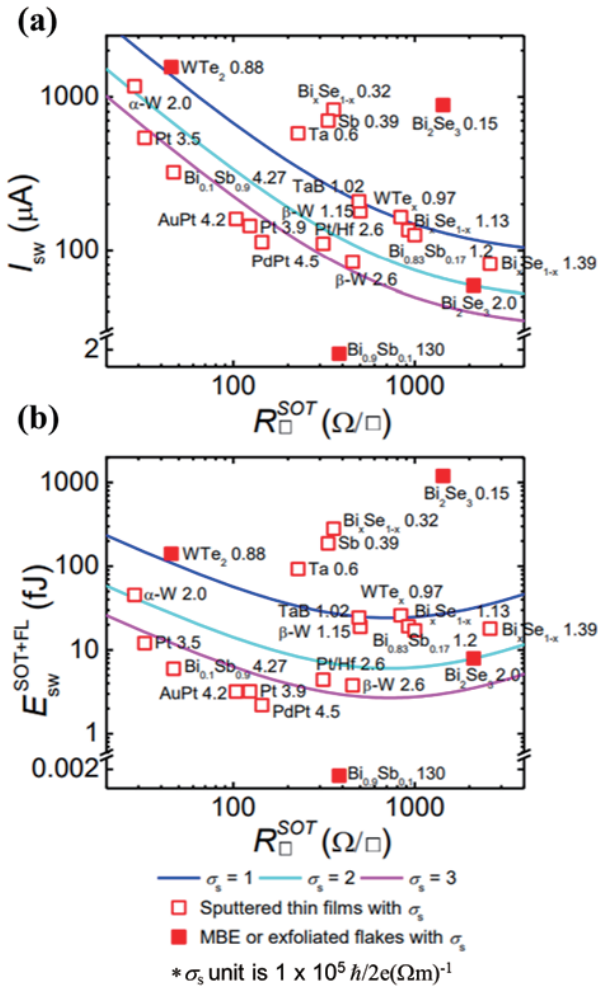

Fig. 8. (a) Switching current and (b) switching energy of SOT-MRAM using various materials as pure spin current source, plotted against their sheet resistance.[38]

Acknowledgements The work on MBE-grown BiSb thin films was conducted in collaboration with Y. Ueda, N.H. D. Khang, and K. Yao and was supported by a Grant-in-Aid for Challenging Exploratory Research from MEXT (No. 16K14228).

References

1) Y. Kato, R. C. Myers, A. C. Gossard, and D. D. Awschalom: *Science*, **306**, 1910 (2004).
2) J. Wunderlich, B. Kaestner, J. Sinova, and T. Jungwirth: *Phys. Rev. Lett.*, **94**, 047204 (2005).
3) K. Garello, C. O. Avci, I. M. Miron, M. Baumgartner, A. Ghosh, S. Auffret, O. Boulle, G. Gaudin, and P. Gambardella: *Appl. Phys. Lett.*, **105**, 212402 (2014).
4) K. Garello, F. Yasin, H. Hody, S. Couet, L. Souriau, S.-H. Sharifi, J. Swerts, R. Carpenter, S. Rao, K. Sethu, J. Wu, D. Crotti, A. Furnémont, G.-S. Kar, W. Kim, M. Pak, and N. Jossart: *2019 Symposium on VLSI Technology*, JFS4-5 (2019).
5) Q. Hao and G. Xiao: *Phys. Rev. Appl.*, **3**, 034009 (2015).
6) J. Sinova, S. O. Valenzuela, J. Wunderlich, C. H. Back, and T. Jungwirth: *Rev. Mod. Phys.*, **87**, 1213 (2015).
7) S. Murakami, N. Nagaosa, and S.-C. Zhang: *Science* **301**, 1348 (2003).
8) D. J. Thouless, M. Kohmoto, M. P. Nightingale, and M. den Nijs: *Phys. Rev. Lett.*, **49**, 405 (1982).
9) F. D. M. Haldane: *Phys. Rev. Lett.*, **61**, 2015 (1988).
10) B.A. Bernevig, T. L. Hughes, and Sh.-Ch. Zhang: *Science*, **314**, 1757 (2006).
11) M. Konig, S. Wiedmann, C. Brüne, A. Roth, H. Buhmann, L. W. Molenkamp, X.-L. Qi, and S.-C. Zhang: *Science*, **318**, 766 (2007).
12) J. E. Moore and L. Balents: *Phys. Rev. B*, **75**, 121306(R) (2007).
13) L. Fu and C.L. Kane: *Phys. Rev. B*, **76**, 045302 (2007).
14) D. Hsieh, D. Qian, L. Wray, Y. Xia, Y. S. Hor, R. J. Cava, and M. Z. Hasan: *Nature*, **452**, 970 (2008).
15) D. Hsieh, Y. Xia, L. Wray, D. Qian, A. Pal, J. H. Dil, J. Osterwalder, F. Meier, G. Bihlmayer, C. L. Kane, Y. S. Hor, R. J. Cava, and M. Z. Hasan: *Science*, **323**, 1106 (2009).
16) H. Zhang, C.-X. Liu, X.-L. Qi, X. Dai, Z. Fang, and S.-C. Zhang: *Nat. Phys.*, **5**, 438 (2009).
17) Y. Xia, D. Qian, D. Hsieh, L. Wray, A. Pal, H. Lin, A. Bansil, D. Grauer, Y. S. Hor, R. J. Cava, and M. Z. Hasan: *Nat. Phys.*, **5**, 398 (2009).
18) Y. L. Chen, J. G. Analytis, J.-H. Chu, Z. K. Liu, S.-K. Mo, X. L. Qi, H. J. Zhang, D. H. Lu, X. Dai, Z. Fang, S. C. Zhang, I. R. Fisher, Z. Hussain, and Z.-X. Shen: *Science*, 3**25**, 178 (2009).
19) D. Hsieh, Y. Xia, D. Qian, L. Wray, F. Meier, J. H. Dil, J. Osterwalder, L. Patthey, A. V. Fedorov, H. Lin, A. Bansil, D. Grauer, Y. S. Hor, R. J. Cava, and M. Z. Hasan: *Phys. Rev. Lett.*, **103**, 146401 (2009).
20) T. Arakane, T. Sato, S. Souma, K. Kosaka, K. Nakayama, M. Komatsu, T. Takahashi, Z. Ren, K. Segawa, and Y. Ando: *Nat. Commun.*, **3**, 636 (2012).
21) C. Z. Zhang, J. Zhang, X. Feng, J. Shen, Z. Zhang, M. Guo, K. Li, Y. Ou, P. Wei, L.-L. Wang, Z.-Q. Ji, Y. Feng, S.H. Ji, X. Chen, J.F. Jia, X. Dai, Z. Fang, S.-C. Zhang, K. He., Y.Y. Wang, L. Lu, X.-C. Ma, Q.-K. Xue: *Science*, **340**, 167 (2013).
22) A. R. Melnik, J. S. Lee, A. Richardella, J. L. Grab, P. J. Mintun, M. H. Fischer, A. Vaezi, A. Manchon, E.-A. Kim, N. Samarth, and D. C. Ralph: *Nature*, **511**, 449 (2014).
23) Y. Wang, P. Deorani, K. Banerjee, N. Koirala, M. Brahlek, S.S. Oh, and H.S. Yang: *Phys. Rev. Lett.*, **114**, 257202 (2015).
24) Y. Wang, D.P. Zhu, Y. Wu, Y.M. Yang, J.W. Yu, R. Ramaswamy, R. Mishra, S.Y. Shi, M. Elyasi, K.-L. Teo, Y.H. Wu, and H.S. Yang: *Nat. Commun.*, **8**, 1364 (2017).
25) J. Zhang, C.-Z. Chang, Z.C. Zhang, J. Wen, X. Feng, K. Li, M.H. Liu, K. He, L.L. Wang, X. Chen, Q.-K. Xue, X.C. Ma, and Y. Wang: *Nat.* Commun., **2**, 574 (2011).
26) Y. Fan, P. Upadhyaya, X.F. Kou, M.R. Lang, S. Takei, Z.X. Wang, J.S. Tang, L. He, L.-T. Chang, M. Montazeri, G.Q. Yu, W.J. Jiang, T.X. Nie, R. N. Schwartz, Y. Tserkovnyak, K. L. Wang: *Nat. Mater.*, **13**, 699 (2014).
27) K. Yasuda, A. Tsukazaki, R. Yoshimi, K. Kondou, K. S. Takahashi, Y. Otani, M. Kawasaki, and Y. Tokura: *Phys. Rev. Lett.*, **119**, 137204 (2017).
28) J. Han, A. Richardella, S. A. Siddiqui, J. Finley, N. Samarth, and L. Liu : *Phys. Rev. Lett.*, **119**, 077702 (2017).
29) H. Wu, P. Zhang, P. Deng, Q. Lan, Q. Pan, S. A. Razavi, X.

Che, L. Huang, B. Dai, K. Wong, X. Han, and K. L. Wang: *Phys. Rev. Lett.*, **123**, 207205 (2019).
30) P. N. Hai: *Bulletin of Solid State Physics and Applications (JSAP)*, **25(5)**, 173 (2019).
31) Y. Ueda, N. H. D. Khang, K. Yao, and P. N. Hai: *Appl. Phys. Lett.*, **110**, 062401 (2017).
32) N.H.D. Khang, Y. Ueda, K, Yao, and P. N. Hai: *J. Appl. Phys.*, **122**, 143903 (2017).
33) N.H.D. Khang, Y. Ueda, and P. N. Hai: *Nat. Mater.*, **17**, 808 (2018).
34) X.-G. Zhu, M. Stensgaard, L. Barreto, W. S. e Silva, S. Ulstrup, M. Michiardi, M. Bianchi, M. Dendzik, and P. Hofmann: *New J. Phys.*, **15**, 103011 (2013).
35) R. Ranijbar, K. Z. Suzuki, Y. Sasaki, L. Bainsla, and S. Mizukami: *Jpn. J. Appl. Phys.*, **55**, 120302 (2016).
36) K. K. Meng, J. Miao, X. G. Xu, Y. Wu, J. Xiao, J. H. Zhao, and Y. Jiang: *Sci. Rep.*, **6**, 38375 (2016).
37) K. K. Meng, J. Miao, X. G. Xu, Y. Wu, X. P. Zhao, J. H. Zhao, and Y. Jiang: *Phys. Rev. B*, **94**, 214413 (2014).
38) X. Li, S.-J. Lin, Mahendra Dc, Y.-C. Liao, C.Y. Yao, A. Naeemi, W. Tsai, and S. X. Wang: *IEEE J. Electron Devi.*, **8**, 674 (2020).
39) Mahendra DC, R. Grassi, J.-Y. Chen, M. Jamali, D. R. Hickey, D. Zhang, Z.Y. Zhao, H.S. Li, P. Quarterman, Yang Lv, M. Li, A. Manchon, K. A. Mkhoyan, T. Low, and J.-P. Wang: *Nat. Mater.*, **17**, 800 (2018).
40) T. Fan, M. Tobah, T. Shirokura, N. H. D. Khang, and P. N. Hai: *Jpn. J. Appl. Phys.*, **59**, 063001 (2020).
41) N. H. D. Khang, S. Nakano, T. Shirokura, Y. Miyamoto, and P. N. Hai: *Sci. Rep.*, **10**, 12185 (2020).

Received May. 31, 2020; Revised Sep. 2, 2020; Accepted Sep. 3, 2020

Journal of the Magnetics Society of Japan

Vol. 44 No. 6 (通巻第 312号) 2020年11月1日発行

Vol. 44 No. 6 Published Nov. 1, 2020
by the Magnetics Society of Japan
Tokyo YWCA building Rm207, 1–8–11 Kanda surugadai, Chiyoda-ku, Tokyo 101–0062
Tel. +81–3–5281–0106 Fax. +81–3–5281–0107

Printed by JP Corporation Co., Ltd.
Sports Plaza building 401, 2–4–3, Shinkamata Ota-ku, Tokyo 144–0054
Advertising agency: Kagaku Gijutsu-sha

発行：（公社）日本磁気学会 101–0062 東京都千代田区神田駿河台 1–8–11 東京YWCA会館 207 号室
製作：ジェイピーシー 144–0054 東京都大田区新蒲田 2–4–3 スポーツプラザビル401 Tel.（03）6715–7915
広告取扱い：科学技術社 111–0052 東京都台東区柳橋 2–10–8 武田ビル 4F Tel.（03）5809–1132